ACS APPLIED MATERIALS & INTERFACES

Research Article

Cite This: ACS Appl. Mater. Interfaces 2019, 11, 15881−15890

www.acsami.org

Surface Functionalization of Grown-on-Tip ZnO Nanopyramids: From Fabrication to Light-Triggered Applications

Alberto Gasparotto,*[,†] Chiara Maccato,[†] Giorgio Carraro,[†] Cinzia Sada,[‡] Urška Lavrenčič Štangar,[§,∥] Bruno Alessi,[⊥] Conor Rocks,[⊥] Davide Mariotti,[⊥] Andrea La Porta,[#] Thomas Altantzis,[#] and Davide Barreca[&]

[†]Department of Chemical Sciences and [‡]Department of Physics and Astronomy, Padova University and INSTM, 35131 Padova, Italy

[§]Faculty of Chemistry and Chemical Technology, University of Ljubljana, 1000 Ljubljana, Slovenia

[∥]Laboratory for Environmental and Life Sciences, University of Nova Gorica, 5000 Nova Gorica, Slovenia

[⊥]Nanotechnology & Integrated Bio-Engineering Centre (NIBEC), Ulster University, Newtownabbey BT37 0QB, U.K.

[#]EMAT, University of Antwerp, 2020 Antwerpen, Belgium

[&]CNR-ICMATE and INSTM, Department of Chemical Sciences, Padova University, 35131 Padova, Italy

Supporting Information

ABSTRACT: We report on a combined chemical vapor deposition (CVD)/radio frequency (RF) sputtering synthetic strategy for the controlled surface modification of ZnO nanostructures by Ti-containing species. Specifically, the proposed approach consists in the CVD of grown-on-tip ZnO nanopyramids, followed by titanium RF sputtering under mild conditions. The results obtained by a thorough characterization demonstrate the successful ZnO surface functionalization with dispersed Ti-containing species in low amounts. This phenomenon, in turn, yields a remarkable enhancement of photoactivated superhydrophilic behavior, self-cleaning ability, and photocatalytic performances in comparison to bare ZnO. The reasons accounting for such an improvement are unravelled by a multitechnique analysis, elucidating the interplay between material chemico-physical properties and the corresponding functional behavior. Overall, the proposed strategy stands as an amenable tool for the mastering of semiconductor-based functional nanoarchitectures through *ad hoc* engineering of the system surface.

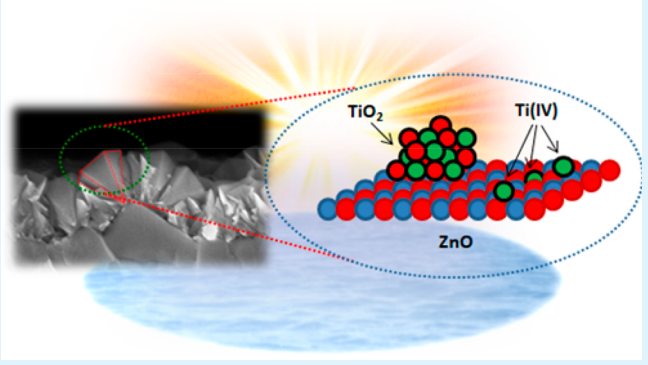

KEYWORDS: *ZnO-based nanomaterials, surface engineering, photoinduced superhydrophilicity, self-cleaning, photocatalysis*

INTRODUCTION

ZnO, similarly to TiO_2, is an important n-type semiconductor that, due to its appealing optoelectronic and structural properties, has been widely studied for photocatalytic, self-cleaning, and other light-triggered applications.[1−8] In this regard, examples on the use of ZnO-based materials encompass various fields, ranging from water and air photocatalytic purification[2−4,9−11] and solar fuels generation by photocatalytic/photoelectrochemical routes[12−16] to the conversion of radiant energy into electricity in dye-sensitized solar cells[17−19] and up to the fabrication of smart surfaces with antifogging properties.[2,3,5]

Notwithstanding the impressive research efforts devoted to zinc(II) oxide, technological advancements based on the use of ZnO systems are still hindered by some material limitations, among which are the moderate catalytic activity, the rapid recombination of photogenerated charge carriers, and the tendency to photocorrosion.[12,20−22] To overcome such drawbacks, two main strategies have been proposed:[4,11,20,23,24] (i) the fabrication of composites based on the combination of ZnO with other semiconductors and (ii) the modification of ZnO by doping with foreign elements. In this context, ZnO−TiO_2 composites and Ti(IV)-doped ZnO are appealing systems to address issues i) and ii), respectively, resulting in nanomaterials with improved functional performances. In fact, ZnO−TiO_2 composites combine the remarkable TiO_2 reactivity and high ZnO electron mobility with the generation of new active sites resulting from the interactions between the two oxides.[13,18,19,25−27] In addition, ZnO coupling with TiO_2 yields an improved photocorrosion resistance, induces the

Received: January 7, 2019
Accepted: April 9, 2019
Published: April 18, 2019

DOI: 10.1021/acsami.8b22744
ACS Appl. Mater. Interfaces 2019, 11, 15881−15890

passivation of surface recombination sites, and might enhance the separation of photogenerated charge carriers.[4,13,15−17,23,26−29] In this regard, it is worth highlighting that ZnO readily forms a variety of high surface area nanostructures that stand as attractive platforms for photocatalytic reactions and other light-triggered applications (e.g., self-cleaning and antifogging) strongly dependent on surface properties.[2,5,6,13] Albeit ZnO nanoarchitectures are characterized by a light absorbing volume smaller than compact ZnO systems, this effect is typically counterbalanced by various beneficial phenomena, such as a higher active area maximizing the contact with the reaction environment, the possibility to tailor light harvesting and charge transport, the occurrence of anisotropic properties, and the opportunity to efficiently functionalize ZnO with foreign elements or surface activators, yielding an intimate contact between the system components.[2,5,6,26]

Despite ZnO−TiO_2 composites have been fabricated by various investigators, the majority of works has so far been focused on systems containing a relatively similar amount of the two oxides.[9,10,12,16,23,24,28,30] The resulting coupled materials often suffer from a poor control over particle morphology, interface quality, and compositional homogeneity, hampering thus a deeper understanding of structure−property relationships and the consequent optimization of functional performances. In a different way, only a few papers have reported on the tailored surface functionalization of ZnO by an ultrathin (<5 nm) TiO_2 conformal layer or by functionalization with a low amount of TiO_2 nanoparticles.[13,17,18,31] It is worthwhile noticing that the use of an ultrathin shell layer is particularly desirable for light-triggered applications, since it offers a minimized charge carrier diffusion distance to the outermost surface.[13] Alternatively, the controlled dispersion of tiny TiO_2 particles on ZnO results in the exposure of a composite surface characterized by the presence of ZnO/TiO_2 heterojunctions, an important goal to maximize interfacial synergistic effects originating from the coupling of the two oxides.[2,32]

To date, zinc oxide doping by various metals and nonmetals has been successfully reported to increase ZnO light harvesting properties, introduce reactive centers on its surface, and suppress charge carrier recombination.[20,21,33−37] In this regard, whereas surface dopants in proper amounts boost the system photocatalytic performances, bulk doping turns out to be unfavorable, since it typically acts in the opposite direction.[21,34,36,38,39] So far, ZnO doping by Ti(IV) centers has been scarcely explored, especially if compared to the use of ZnO−TiO_2 composites.[37,40,41] Taken together, the above observations highlight that the full exploitation of ZnO−TiO_2 and Ti-doped ZnO potential depends on the availability of synthetic tools enabling a direct control over local composition, morphology, exposed crystal facets, defectivity, and interface quality.[2,42−44]

Recently, we have reported on the CVD fabrication of ZnO nanopyramids grown on their tips, with the ⟨001⟩ crystallographic direction oriented perpendicularly to the used Si(100) substrates.[45] The resulting porous nanopyramid arrays were likely endowed with a high surface area and predominantly exposed high surface energy (001) and (101) reactive facets.[22,46−48] Based on these favorable features, in this study we focus our attention on the CVD growth of ZnO nanopyramids on fluorine-doped tin oxide (FTO) substrates and their subsequent functionalization with Ti-containing species via RF sputtering.

Overall, under the adopted sputtering conditions, much softer than those typically reported in the literature for sputtering experiments,[10,19,49−51] the low Ti deposition rate and the reduced energy of sputtered species impinging onto ZnO surface allowed to (a) prevent any undesired ZnO morphology alteration, (b) selectively decorate the surface of ZnO nanostructures with very small titanium amounts, and (c) control the dispersion of Ti-containing species and their aggregation into TiO_2 particles through heterogeneous nucleation and growth processes.

The controlled and simultaneous introduction of TiO_2 and Ti(IV) species impacted very favorably on material photoinduced superhydrophilic behavior, self-cleaning properties, and liquid phase photocatalytic activity. In this work, we present and discuss the results achieved by a thorough characterization of the obtained materials, elucidating the main reasons accounting for the improved characteristics of functionalized zinc oxide systems with respect to bare ZnO.

EXPERIMENTAL SECTION

Synthesis. ZnO depositions were performed in a previously described CVD apparatus consisting of a tubular furnace equipped with a quartz tube hot-wall reactor.[2] $Zn(hfa)_2$TMEDA (hfa = 1,1,1,5,5,5-hexafluoro-2,4-pentanedionate; TMEDA = *N*,*N*,*N*′,*N*′-tetramethylethylenediamine)[52] was used as Zn precursor. The compound was heated at 80 °C in an external vessel, and its vapors were delivered to the reaction chamber by a 100 sccm N_2 flow through gas lines maintained at 120 °C to prevent condensation phenomena. An additional O_2 flow (rate = 30 sccm) was separately supplied to the reactor after passing through a water reservoir kept at 30 °C. For each deposition, suitably cleaned[2] 1 × 2 cm^2 FTO-coated glass substrates (Aldrich, ≈7 Ω/sq, FTO thickness = 600 nm) were placed at the center of the reactor, which was maintained at 350 °C at a total operating pressure of 3.0 mbar (deposition time = 2 h), according to previously optimized experimental conditions.[45]

For the preparation of Ti-modified samples, the above ZnO matrices were fixed on the grounded electrode of a plasmochemical reactor equipped with a RF generator (ν = 13.56 MHz).[2] Experiments were performed using electronic grade Ar plasmas, after mounting a Ti target (Alfa Aesar, purity = 99.95%, thickness = 0.3 mm, diameter = 2 in.) on the RF electrode. Deposition durations of 2 or 4 h (samples ZnO-Ti(2 h) and ZnO-Ti(4 h), respectively) were used to tailor the overall titanium content in the ZnO deposits, while keeping constant the following parameters: Ar flow rate = 10 sccm; total pressure = 0.3 mbar; RF power = 20 W; grounded electrode temperature = 60 °C. Under the adopted conditions, the titanium deposition rate was estimated to be ≤1 nm/h based on preliminary calibration experiments.

Characterization. Field emission-scanning electron microscopy (FE-SEM) analyses were performed by a Zeiss SUPRA 40 VP instrument, using a primary electron beam voltage of 20.0 kV. ImageJ software was used to evaluate the mean aggregate dimensions and deposit thickness by averaging over various independent measurements.

X-ray diffraction (XRD) patterns were collected at a fixed incidence angle of 1.0° by means of a Bruker D8 Advance instrument equipped with a Göbel mirror, using a Cu Kα X-ray source operating at 40 kV and 40 mA.

Atomic force microscopy (AFM) analyses were performed by an NT-MDT SPM solver P47H-PRO apparatus, operating in semicontact mode and in air. Root-mean-square (rms) roughness values were obtained from 3 × 3 μm^2 images after background subtraction.

Secondary ion mass spectrometry (SIMS) analyses were performed by a IMS 4f mass spectrometer (Cameca), using a Cs^+ primary ion beam (voltage = 14.5 keV; current = 30 nA, stability = 0.3%) and

DOI: 10.1021/acsami.8b22744
ACS Appl. Mater. Interfaces 2019, 11, 15881−15890

negative secondary ion detection, adopting an electron gun for charge compensation. The beam scanned area was 150 × 150 μm^2, and secondary ions were collected from a 7 × 7 μm^2 sub-region to prevent detrimental crater effects.

X-ray photoelectron spectroscopy (XPS) measurements were performed on a PerkinElmer Φ 5600ci spectrometer with a standard Al Kα excitation source (1486.6 eV). Binding energy (BE) values (uncertainty = ±0.1 eV) were corrected for charging effects by assigning to the C 1s peak of adventitious carbon a BE of 284.8 eV.[45,53] After a Shirley-type background subtraction, atomic compositions were evaluated using Φ V5.4A sensitivity factors.

Samples for cross-sectional transmission electron microscopy (TEM) observations were prepared by mechanical polishing, using an Allied Multiprep system with diamond-lapping films, down to a thickness of ≈20 μm, followed by Ar^+ ion milling by using a Leica EM RES102 apparatus (acceleration voltages up to 4 kV; incident beam angles 6°−11°). Low- and high-magnification high angle annular dark field scanning TEM (HAADF-STEM) images, as well as energy dispersive X-ray spectroscopy (EDXS) elemental maps, were acquired using an aberration corrected cubed FEI Titan instrument operated at 300 kV, equipped with the ChemiSTEM system.[54] HAADF-STEM imaging was performed using probe convergence and detector inner collection semiangles of 21 and 55 mrad, respectively.

UV−vis absorption spectra (resolution = 1 nm) were collected by a PerkinElmer Lambda 650S spectrophotometer equipped with a halogen lamp and a 150 mm integrating sphere by measuring (i) combined transmittance and reflectance by placing the sample at the center of the integrating sphere and (ii) transmittance only by placing the sample at the entrance of the sphere; a quartz sample was used as reference. This allowed us to determine the absorption coefficient taking into account any possible effect due to reflectance changes. Band gap (E_G) values were extrapolated by plotting the absorption coefficient as a function of photon energy, assuming the occurrence of direct allowed transitions.[2,33,41] Optical penetration depth values[55] were calculated at 3.7 eV.

Valence band (VB) XPS spectra were recorded with a Kratos Axis Ultra DLD spectrometer equipped with an Al Kα X-ray source, using an analyzer pass energy of 20 eV. For each sample, three measurement spots were taken (spot size = 400 μm^2).

The absolute Fermi energy was evaluated by Kelvin probe (KP) measurements in air (KP Technologies APS04) with a 2 mm gold plated tip. A sputtered Au-on-Si reference was adopted to calibrate the tip work function. Specimens were stored in the dark for 24 h prior to each measurement. Fermi energy values were subsequently obtained scanning over a 4 mm × 4 mm area and averaging the obtained data to the final value.

Functional Tests. Water contact angle (WCA) measurements were performed as a function of UV-A irradiation time in a photochamber equipped with three lamps (Actinic BL, Philips, 2 × 20 W and 1 × 40 W, wavelength range 350−400 nm, with λ_{max} = 370 nm, optical energy density = 2.2 mW/cm^2) using a Theta Lite (Biolin Scientific) instrument.[56] For each irradiation time, five drops were deposited on different sample regions and the corresponding WCA values were statistically averaged. The atmosphere in the test chamber was ambient air. Prior to water contact angle tests, samples were stored in the dark for nearly one month.

For the evaluation of self-cleaning activity, specimens were dip-coated in a 0.2 M methyl stearate solution in hexane (withdrawal rate = 10 cm/min) and subsequently dried in air.[56] Similarly to the standard method ISO 27448 indicating oleic acid as a model fatty compound,[57,58] methyl stearate was used to mimic the presence of dirt and its light-assisted degradation under controlled laboratory conditions.[5,6,59] The degradation of the resulting solid organic layer was then followed by monitoring the WCA time evolution upon UV-A irradiation in the above-described apparatus.[60]

Liquid-phase photocatalytic activity was investigated by analyzing the photodegradation of the Plasmocorinth B dye in a homemade UV photoreactor.[61] For each experiment, two identical samples (total geometrical surface = 25 cm^2) were immersed into 50 mL of a dye aqueous solution (concentration = 12 mg/L) in the central cell surrounded by six UV-A lamps (Blacklight Blue, Philips, 36 W/m^2). An O_2 flow (100 mL/min) was bubbled in the solution, and the dye concentration was spectrophotometrically determined (Agilent Cary 60 UV−vis spectrophotometer) by monitoring the dye absorbance maximum (λ_{max} = 527 nm) upon irradiation at regular time intervals.[56]

RESULTS AND DISCUSSION

In this study, the CVD growth of ZnO nanopyramids on FTO substrates was followed by their surface functionalization with Ti-containing species via RF sputtering for different process durations (2 or 4 h) to tailor the overall Ti content in the obtained systems.

FE-SEM morphological analysis (Figure 1a) revealed the formation of ZnO nanopyramid arrays with downward pointing tips, in line with the results recently reported for the growth of analogous systems on Si(100) substrates.[45] Yet, in the present case, the inherent FTO substrate corrugation

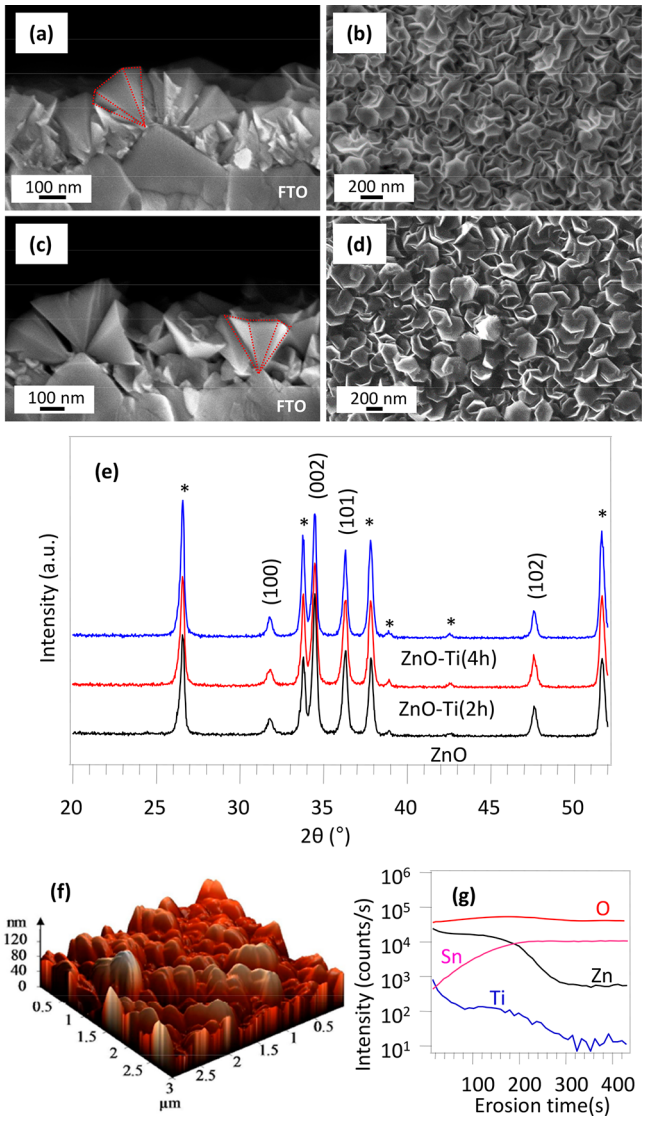

Figure 1. Cross-sectional and plane view FE-SEM micrographs of (a, b) bare ZnO and (c, d) ZnO-Ti(2h) specimens. (e) XRD patterns for ZnO and ZnO-Ti samples. Reflections pertaining to the FTO substrate are marked by asterisks. Representative AFM micrograph (f) and SIMS depth profile (g) of ZnO and ZnO-Ti(2h), respectively.

DOI: 10.1021/acsami.8b22744
ACS Appl. Mater. Interfaces 2019, 11, 15881−15890

resulted in the formation of more disordered deposits than the previously reported ones.

The lateral size of ZnO nanostructures progressively increased from the interface with the substrate up to the outermost surface, yielding a plane-view texture characterized by the even interconnection of pyramid hexagonal bases (Figure 1b). The average deposit thickness was 250 ± 20 nm, whereas the ZnO pyramid base had a mean size of 220 ± 10 nm.

Upon functionalization, the system morphology did not undergo significant variations (Figure 1c,d), indicating that the soft conditions adopted for titanium sputtering enabled to preserve the original ZnO morphology. An inspection of the recorded images yielded no clear evidence of titanium-containing aggregates, suggesting that the latter were present in very low amount and/or as highly dispersed species. Accordingly, XRD patterns of bare ZnO and ZnO-Ti samples were almost identical irrespective of Ti sputtering time and, apart from the substrate signals, presented only reflections attributable to hexagonal ZnO (wurtzite) (Figure 1e).[62] In this regard, the high relative intensity of the (002) signal indicated that nanopyramids grew along the ⟨001⟩ crystallographic direction, as confirmed by HAADF-STEM analyses (see below). In line with FE-SEM results, AFM investigation revealed a very similar surface topography (Figure 1f and Figure S1a) for all specimens, with an average rms roughness value of 22 ± 2 nm.

To evaluate the mutual in-depth distribution of zinc and titanium, SIMS analyses were undertaken (Figure 1g and Figure S1b). As can be observed, Zn and Ti ionic yields displayed an almost parallel trend throughout the investigated depth, indicating a uniform distribution of titanium into ZnO.

As a matter of fact, the trend of titanium ionic yield could be traced back to the efficient surface functionalization of ZnO nanopyramids by Ti-containing species (whose nature will be discussed in more detail below) dispersed throughout the whole deposit. The successful achievement of this goal, which has a positive impact on material performances (see below), results from the synergistic combination of the intrinsic ZnO porosity and the inherent sputtering infiltration power.[2,53,63,64] The deposit−FTO interface was significantly broadened, resulting in an apparent tin diffusion into the target material, a phenomenon which was traced back to the inherent FTO roughness and the high porosity of ZnO nanopyramid arrays.

Taken together, the above results revealed that irrespective of the sputtering duration, ZnO-Ti specimens possessed similar structural and morphological features, but a different overall Ti content, as suggested by SIMS depth profiles. Since the overall Ti/Zn ratio plays an important role on functional properties and catalytic performances,[27,30] quantification of this parameter was attempted by EDXS. Nevertheless, the very low amount of titanium did not allow reliable measurements, suggesting that the overall titanium content was close to or below EDXS detection limit (ca. 0.1 wt %). In this regard, at variance from a large part of the existing literature, our research work aimed at investigating ZnO surface modification by very low amounts of Ti-containing species and their interplay with the resulting functional properties, an issue which has not been thoroughly investigated up to date. Because of the above limitations of the EDXS technique, in this work we used XPS analyses (see Figure S2) to estimate the Ti/Zn surface atomic ratio, resulting in values of 0.11 and 0.22 for samples ZnO-Ti(2h) and ZnO-Ti(4h), respectively. XPS data also revealed that the Ti $2p_{3/2}$ photoelectron signal for Ti-containing specimens was located at BE = 458.6 eV, indicating that titanium species were present in the IV oxidation state.[1,65,66] At variance with the Ti $2p_{3/2}$ signal, the Zn $2p_{3/2}$ one underwent a small, but measurable, shift to higher BE values upon going from bare ZnO (1021.6 eV) to ZnO-Ti(2h) (1021.8 eV) and finally ZnO-Ti(4h) (1021.9 eV). This phenomenon, which was accompanied by a similar shift of Zn Auger parameters (see the Supporting Information), might be due to the surface doping of zinc oxide by Ti(IV) ions with formation of Zn−O−Ti moieties.[65,67]

To assess the influence of titanium sputtering on ZnO functional properties, the photoinduced hydrophilic behavior of ZnO, ZnO-Ti(2h), and ZnO-Ti(4h) systems was initially investigated by water contact angle measurements (Figure 2a).

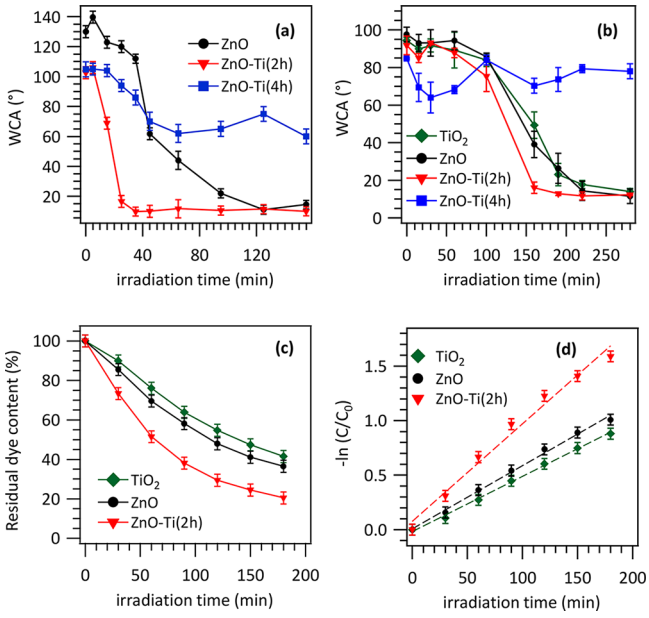

Figure 2. (a) Water contact angle evolution as a function of irradiation time for the samples investigated in the present work. (b) WCA vs irradiation time for methyl stearate-coated systems. A reference TiO_2 sample, prepared by titanium sputtering (4 h) directly on FTO, was also tested for comparison. (c) Plasmocorinth B photocatalytic degradation promoted by the target specimens and (d) corresponding logarithmic plots.

As can be observed, bare ZnO displayed a relatively slow hydrophobic-to-hydrophilic conversion upon UV light irradiation. This phenomenon was traced back to the light assisted generation of hydroxyl groups and concomitant photocatalytic degradation of adventitious organic species adsorbed on the semiconductor surface.[2,3,5,68] Interestingly, the sample ZnO-Ti(2h) reached superhydrophilic WCA values (i.e., WCA < 10°, see also Figure S3a) with a much faster kinetics, outperforming even a commercial Pilkington Activ Glass used as a standard reference for similar applications.[6] Cyclability tests revealed very similar performances during the first two utilization cycles (Figure S4), suggesting a good material stability upon operation.

Nevertheless, when the sputtering time was increased to 4 h (sample ZnO-Ti(4h)), resulting in a higher Ti content, a severe worsening of the system behavior took place, indicating that titanium loading has to be carefully controlled to tailor the system functional properties.

DOI: 10.1021/acsami.8b22744
ACS Appl. Mater. Interfaces 2019, 11, 15881−15890

The self-cleaning behavior of the target nanosystems was tested in the photodecomposition of methyl stearate, a model fatty compound, through measurements of WCA values vs illumination time. As can be observed in Figure 2b, the initial WCA values underwent a progressive decrease upon irradiation, in line with the fatty compound decomposition,[6] yielding ultimately a hydrophilic surface for ZnO and ZnO-Ti(2h). The latter was the best performing sample, whereas ZnO and TiO_2 featured a slightly lower degradation efficiency, and ZnO-Ti(4h) did not show any significant activity.

Subsequently, samples were also tested in the liquid phase photocatalytic oxidation of Plasmocorinth B, whose concentration was monitored by UV−vis spectroscopy (Figure S3b). In line with the above results, ZnO-Ti(2h) displayed a significantly faster dye degradation than bare ZnO and TiO_2 (Figure 2c). The dye photodecomposition followed a first-order reaction kinetics (Figure 2d),[56] with rate constants (in min^{-1}) decreasing in the order 9.0×10^{-3} (ZnO-Ti(2h)), 5.8×10^{-3} (ZnO), and 5.1×10^{-3} (TiO_2). The obtained values compared very favorably with previously reported data[61] thanks to the unique features of the present deposits, combining a porous morphology with the exposure of particularly reactive ZnO crystallographic surfaces.[22,46,48]

To elucidate the main phenomena underlying the best performances of sample ZnO-Ti(2h), HAADF-STEM and EDXS analyses were carried out. In line with FE-SEM results (see above), low-magnification HAADF-STEM imaging (Figure 3a) evidenced the presence of a homogeneous ZnO nanopyramid array on the top of the FTO layer. No epitaxial relationship between ZnO and FTO could be observed. EDXS elemental maps for Zn, Si, and Sn acquired from the same region (Figure 3b) clearly revealed the distribution of these elements on the ZnO deposit and in the underlying substrate. Conversely, no clear-cut evidence of Ti presence was observed at this magnification, in agreement with the relatively low Ti content (see above). As a consequence, higher resolution HAADF-STEM imaging and EDXS elemental mapping were performed on individual ZnO nanopyramids (Figure 3c), and the results demonstrated that Ti-containing species were very finely dispersed over ZnO nanostructures. More specifically, EDXS analyses in the regions highlighted by the yellow and red boxes in Figure 3c unambiguously confirmed that titanium presence was limited to zinc oxide surface, whereas the underlying ZnO region was Ti-free (compare Figures 3d and 3e). A high-resolution HAADF-STEM image of the region evidenced in green in Figure 3c confirmed the formation of highly crystalline ZnO in the hexagonal wurtzite phase[62] (Figure 3f). More specifically, ZnO nanostructures had a preferential ⟨001⟩ orientation, with the pyramid axis nearly perpendicular to the FTO substrate surface, in line with XRD results. In a different way, titanium sputtering resulted in an amorphous and discontinuous TiO_2 deposit with a thickness of ≈2 nm (Figure 3g). The defect-free crystal structure of ZnO and the features of TiO_2 surface species are better shown in the enlarged high-resolution HAADF-STEM image reported in Figure 4.

For sample ZnO-Ti(4h), obtained with a longer sputtering time, HAADF-STEM analysis (Figure S5) evidenced a titanium dispersion relatively similar to ZnO-Ti(2h). Nevertheless, the higher titanium content yielded an increase of the average TiO_2 thickness (4−5 nm, as revealed by Figure S5c,d), accompanied by a more effective ZnO surface coverage (see also Figure S6). This result is in good agreement with the 2-fold increase of the surface Ti/Zn atomic ratio on going from ZnO-Ti(2h) to ZnO-Ti(4h) (see the above XPS data). It is worth highlighting that due to the size of ZnO crystals and the small difference between Zn and Ti atomic number, HAADF-STEM imaging did not yield clear evidence on the presence of isolated Ti(IV) doping centers, whose occurrence was however

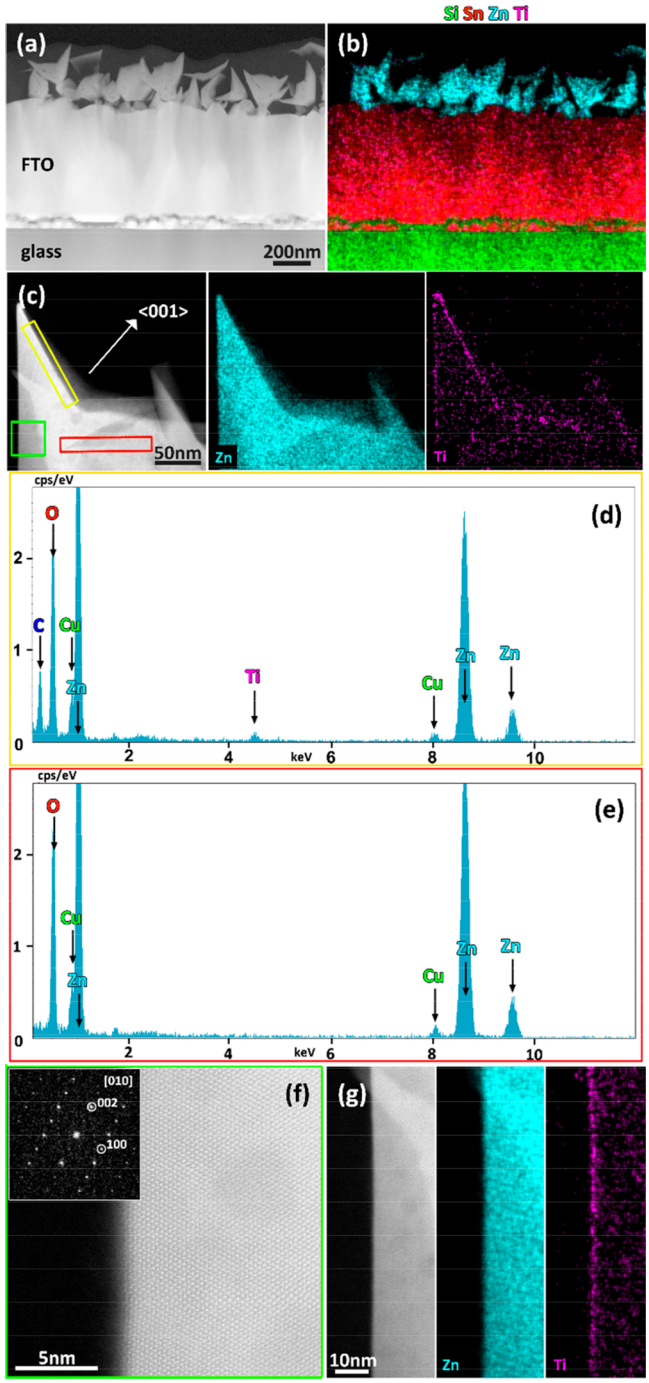

Figure 3. Representative cross-sectional HAADF-STEM image (a) and corresponding EDXS chemical maps (b) for sample ZnO-Ti(2h). (c) HAADF-STEM image and corresponding Zn and Ti EDXS maps for an individual ZnO nanopyramid. (d, e) EDXS spectra acquired from the regions marked in (c) by yellow and red boxes, respectively. (f) High-resolution HAADF-STEM image of the area inside the green rectangle in (c). The inset displays the fast Fourier transform (FFT) pattern corresponding to the [010] zone axis of ZnO. (g) Zn and Ti EDXS maps from the surface region shown in (f).

DOI: 10.1021/acsami.8b22744
ACS Appl. Mater. Interfaces 2019, 11, 15881−15890

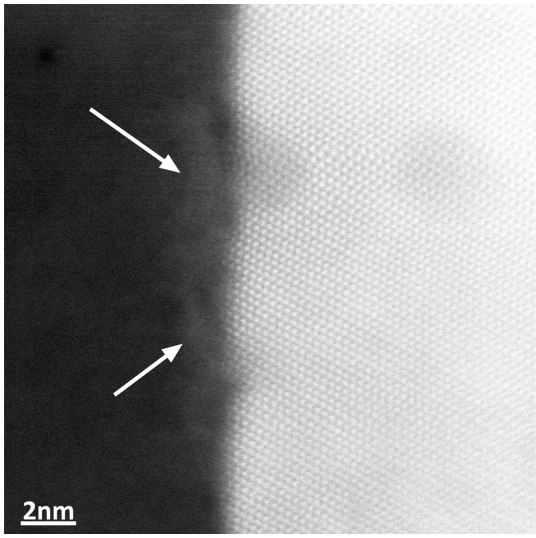

Figure 4. High-resolution cross-sectional HAADF-STEM micrograph of the surface region of specimen ZnO-Ti(2h). Arrows indicate the TiO_2 deposit, while the brighter image region corresponds to ZnO.

suggested by XPS data (see above). To attain a deeper insight into this issue, a detailed study of the specimen optical and electronic properties was undertaken. The most relevant data are displayed in Figure 5 and summarized in Table 1.

Table 1. Optical Band Gap (E_G), Valence Band Maximum (VBM) against the Vacuum Level, Fermi Level Position (E_F), and VBM − E_F Values for ZnO and ZnO-Ti Samples

sample	E_G (eV)	VBM (eV)	E_F (eV)	VBM − E_F (eV)
ZnO	3.29	7.21	4.52	2.69
ZnO-Ti(2h)	3.30	7.63	4.48	3.15
ZnO-Ti(4h)	3.30	7.59	4.47	3.12

Analysis of optical absorption spectra and Tauc plots (Figure 5a and Figure S7) yielded a band gap value close to E_G = 3.30 eV for all samples. Such a result, in excellent agreement with literature data on bare ZnO,[20,24,33,36] enabled to rule out a significant bulk doping of zinc oxide by titanium. Nonetheless, the appreciable increase of the absorption coefficient of Ti-containing samples with respect to bare ZnO (Figure 5a) cannot be explained as a mere overlap of ZnO and TiO_2 optical properties. In fact, ZnO and TiO_2 have a comparable absorption coefficient,[69−73] and the low TiO_2 amount in specimens ZnO-Ti(2h) and ZnO-Ti(4h) cannot motivate the observed increase of α values for $h\nu$ higher than 3.3 eV. As a consequence, the occurrence of isolated Ti(IV) species acting as surface dopants was primarily hypothesized as the main reason accounting for the observed phenomenon. Similar effects have already been reported in the literature for surface-doped semiconductors.[74,75] Interestingly, calculation of the optical penetration depth[55,70] yielded values of ≈200 and 140

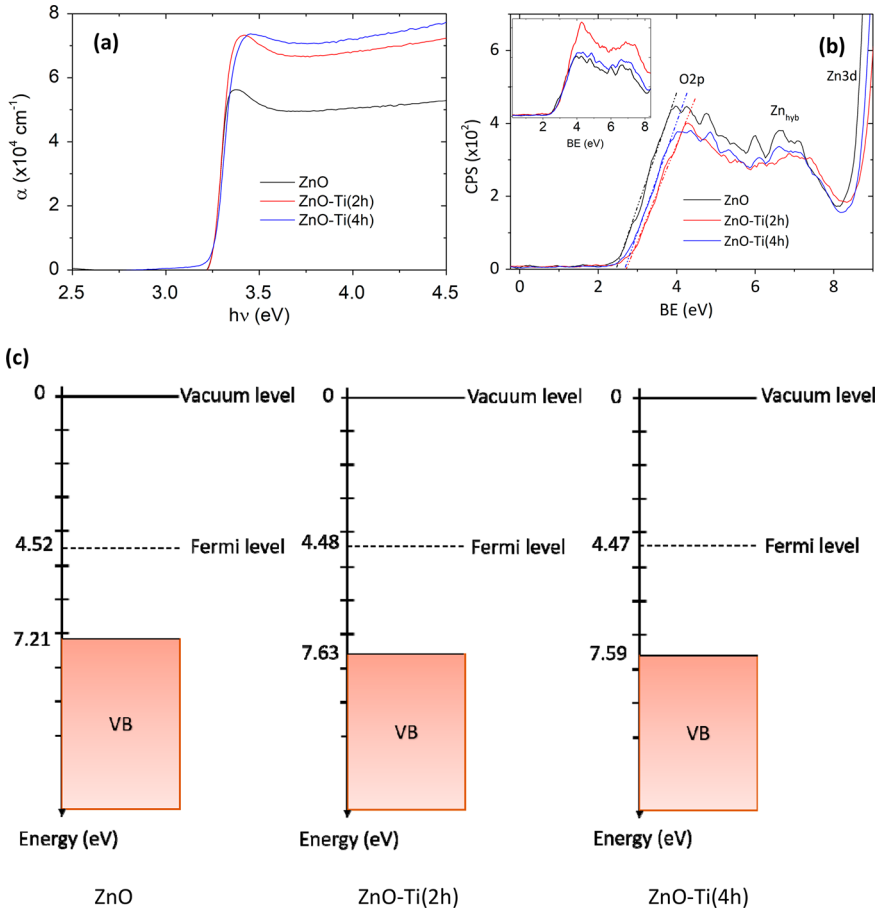

Figure 5. (a) Absorption coefficient vs photon energy for samples ZnO, ZnO-Ti(2h), and ZnO-Ti(4h). (b) XPS valence band scans for the same specimens; the inset shows the same spectra normalized to the Zn 3d peak. (c) Partial energy band diagram for the samples. Valence band edge and absolute Fermi energies were obtained by XPS and KP measurements, respectively.

DOI: 10.1021/acsami.8b22744
ACS Appl. Mater. Interfaces 2019, 11, 15881−15890

nm for bare and Ti-modified ZnO samples, respectively. Taking into account that the average deposit thickness was 250 ± 20 nm (see above), these results indicate that the largest part of the incident radiation is effectively absorbed by the developed ZnO-based nanostructures, beneficially affecting in particular Ti-containing systems.

XPS valence band scans for the target materials are displayed in Figure 5b, and the obtained energy position of valence band maxima against the vacuum level are shown in Figure 5c (see also Table 1). From the former figure, a clear shift of the valence band edge to higher BE values was detected upon Ti introduction, consistent with the sample surface modification. For both bare ZnO and ZnO-Ti(4h) samples, the energy features in Figure 5b were associated with the O 2p orbitals, Zn 3d orbitals, and hybridized Zn−O bonds,[76] whereas the ZnO-Ti(2 h) specimen exhibited a weakly modified electronic structure. Such a difference, better appreciated when the spectra are normalized to the Zn 3d peak (Figure 5b, inset), supports the possible occurrence of ZnO surface doping by Ti(IV) ions for sample ZnO-Ti(2h). This phenomenon could also justify, for the latter specimen, the slightly higher absorption coefficient above the absorption edge with respect to ZnO-Ti(4 h) (see Figure S7).

KP measurements were finally used to estimate the Fermi level of the samples against a gold reference with a known calibrated work function (Table 1). Whereas UV−vis absorption measurements and the pertaining band gap evaluation are directly influenced by the overall nanodeposit thickness, KP and XPS measurements are surface-sensitive and, hence, strongly influenced by the deposition of Ti-containing species. These analyses allowed to obtain a partial energy band diagram of the Ti-modified surface compared to bare ZnO (Figure 5c). These data indicate that both bare and Ti-modified ZnO samples show n-type behavior with the same optical band gap. The valence band edge at the surface of the film is shifted by ≈0.4 eV after titanium sputtering, while the Fermi level energy does not undergo any appreciable change (shift by ≈0.05 eV) for ZnO-Ti specimens (Figure 5c).

The data discussed so far indicate that differently from band gap values, the surface electronic structure and the valence band edge energy are directly influenced by ZnO functionalization with Ti-containing species, especially for sample ZnO-Ti(2h). This effect cannot be caused by O or Zn vacancies and/or ZnO bulk doping by Ti(IV), which would have resulted in the appearance of a tail near the absorption edge.[21,77] It seems therefore likely that Ti(IV) surface doping appreciably occurs for the ZnO-Ti(2h) sample. Conversely, the increased titanium amount in ZnO-Ti(4h) results in the formation of larger TiO_2 aggregates through heterogeneous nucleation and growth processes.[78−80]

The above results may partially explain the improved functional performances of ZnO-Ti(2h). In fact, the valence band shift to more positive potentials detected for the former sample increases the oxidation power of photogenerated holes,[81] with a beneficial effect on both light-triggered superhydrophilicity and photocatalytic properties. The worse performances of ZnO-Ti(4h) with respect to ZnO-Ti(2h) can be traced back not only to the variations in the absorption coefficient and surface electronic structure but also to an excessive coverage of ZnO surface by Ti-containing species.

Overall, the above-described functional properties can be rationalized on the basis of the chemicophysical characteristics of Ti-modified ZnO systems (Figure 6a). The first steps of titanium deposition involve the functionalization of ZnO pyramids by highly dispersed Ti(IV) ions, acting as surface dopants. As the deposition proceeds, the progressive increase of titanium content results in the nucleation and growth of TiO_2 particles, a phenomenon assisted by plasma activation of surface diffusion phenomena.[78−80] As a whole, both the total titanium amount and relative TiO_2 vs Ti(IV) content in the resulting materials can be controlled. On the basis of a comparative analysis of all the obtained results, the enhanced photoinduced superhydrophilic properties, self-cleaning ability, and photocatalytic performances of the sample ZnO-Ti(2h) can be reasonably ascribed to the combination of the following effects (Figure 6b): (i) The efficient dispersion of Ti(IV) centers on ZnO surface improves light absorption,[33] enhances the Lewis acidity of Zn(II), and favors the collection of photogenerated electrons from ZnO, rendering holes more easily available for oxidation processes.[40] Yet, since Ti(IV) sites act as recombination centers at high Ti concentrations, the establishment of an optimal doping level is of key importance.[34,35,40] (ii) ZnO functionalization by TiO_2 particles plays a key role in improving the separation of photogenerated charge carriers, minimizing detrimental recombination phenomena.[1,4,7,14,15,28] Because both superhydrophilicity and photocatalytic oxidation of organic species strongly depend on h^+ availability over ZnO surface, it is however important to avoid an excessive ZnO coverage by TiO_2,[26] as for specimen ZnO-Ti(4h).

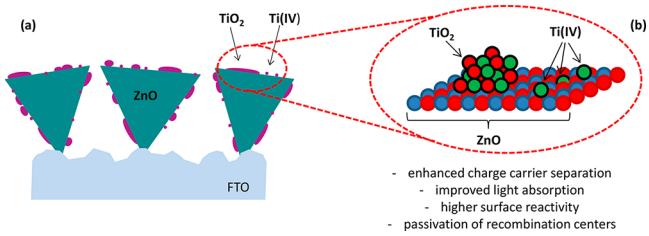

Figure 6. Sketch displaying (a) the distribution of Ti-containing species on ZnO pyramids and (b) the main surface and interface phenomena involved in the light-triggered applications targeted in the present work.

CONCLUSIONS

In this study, an unconventional synthetic strategy for the surface functionalization of supported ZnO nanopyramids with Ti-containing species was developed. The process involved (i) the CVD of grown-on-tip ZnO nanopyramids over FTO substrates and (ii) the RF sputtering of very low Ti amounts over ZnO, adopting particularly mild process conditions. An extensive chemico-physical characterization by means of complementary analytical techniques revealed that the morphology of the pristine ZnO matrices was preserved and that ZnO nanostructure surface was simultaneously decorated by dispersed TiO_2 particles and Ti(IV) centers. In this regard, a careful control of the titanium content afforded a remarkable improvement of the system light-assisted functional properties, as evidenced by photoinduced superhydrophilicity/photocatalytic functional tests, both in the solid and in the liquid phase. The results provided by the developed synthetic approach represent an interesting starting point for future implementations of multifunctional photoactive nanomaterials for smart stimuli-responsive applications and wastewater purification. In this regard, further research efforts will be

DOI: 10.1021/acsami.8b22744
ACS Appl. Mater. Interfaces 2019, 11, 15881−15890

also focused on a detailed structural investigation on the nature of Ti-containing species (possibly under operando conditions) and their time stability upon prolonged use.

■ ASSOCIATED CONTENT

Supporting Information

The Supporting Information is available free of charge on the ACS Publications website at DOI: 10.1021/acsami.8b22744.

Details on AFM, SIMS, XPS, HAADF-STEM, EDXS, and optical absorption experimental data; photographs showing WCA evolution with irradiation time; optical absorption spectra of Plasmocorinth B aqueous solutions as a function of illumination time; WCA as a function of irradiation time during the first two utilization cycles (PDF)

■ AUTHOR INFORMATION

Corresponding Author

*Phone +39-0498275192; e-mail alberto.gasparotto@unipd.it (A.G.).

ORCID

Alberto Gasparotto: 0000-0003-4626-651X
Chiara Maccato: 0000-0001-6368-5754
Urška Lavrenčič Štangar: 0000-0001-9652-2257
Bruno Alessi: 0000-0002-4468-0381
Davide Mariotti: 0000-0003-1504-4383
Thomas Altantzis: 0000-0002-4940-7931
Davide Barreca: 0000-0002-8779-3386

Notes

The authors declare no competing financial interest.

■ ACKNOWLEDGMENTS

The research leading to these results has received financial support from Padova University ACTION postdoc fellowship, DOR 2016-2018, P-DiSC #03BIRD2016-UNIPD projects, and HERALD COST Action MP1402-37831. The support from EPSRC (awards EP/R008841/1 and EP/M024938/1) as well as from the Slovenian Research Agency (research core funding No. P1-0134) is also recognized. T.A. acknowledges a postdoctoral grant from the Research Foundation Flanders (FWO, Belgium). The authors are grateful to Dr. Sebastiano Pianta (Department of Chemical Sciences, Padova University, Italy) for experimental assistance.

■ REFERENCES

(1) Kwiatkowski, M.; Bezverkhyy, I.; Skompska, M. ZnO Nanorods Covered with a TiO_2 Layer: Simple Sol-Gel Preparation, and Optical, Photocatalytic and Photoelectrochemical Properties. *J. Mater. Chem. A* **2015**, *3*, 12748−12760.

(2) Gasparotto, A.; Carraro, G.; Maccato, C.; Sada, C.; Balbuena, J.; Cruz-Yusta, M.; Sánchez, L.; Vodišek, N.; Lavrenčič Štangar, U.; Barreca, D. WO_3-Decorated ZnO Nanostructures for Light-Activated Applications. *CrystEngComm* **2018**, *20*, 1282−1290.

(3) Léonard, G. L. M.; Pàez, C. A.; Ramírez, A. E.; Mahy, J. G.; Heinrichs, B. Interactions between Zn^{2+} or ZnO with TiO_2 to Produce an Efficient Photocatalytic, Superhydrophilic and Aesthetic Glass. *J. Photochem. Photobiol., A* **2018**, *350*, 32−43.

(4) Ramos, P. G.; Flores, E.; Sánchez, L. A.; Candal, R. J.; Hojamberdiev, M.; Estrada, W.; Rodriguez, J. Enhanced Photoelectrochemical Performance and Photocatalytic Activity of ZnO/TiO_2 Nanostructures Fabricated by an Electrostatically Modified Electrospinning. *Appl. Surf. Sci.* **2017**, *426*, 844−851.

(5) Bekermann, D.; Gasparotto, A.; Barreca, D.; Devi, A.; Fischer, R. A.; Kete, M.; Lavrenčič Štangar, U.; Lebedev, O. I.; Maccato, C.; Tondello, E.; Van Tendeloo, G. ZnO Nanorod Arrays by Plasma-Enhanced CVD for Light-Activated Functional Applications. *ChemPhysChem* **2010**, *11*, 2337−2340.

(6) Barreca, D.; Gasparotto, A.; Maccato, C.; Tondello, E.; Lavrenčič Štangar, U.; Patil, S. R. Photoinduced Superhydrophilicity and Photocatalytic Properties of ZnO Nanoplatelets. *Surf. Coat. Technol.* **2009**, *203*, 2041−2045.

(7) Sun, C.; Xu, Q.; Xie, Y.; Ling, Y.; Hou, Y. Designed Synthesis of Anatase-TiO_2 (B) Biphase Nanowire/ZnO Nanoparticle Heterojunction for Enhanced Photocatalysis. *J. Mater. Chem. A* **2018**, *6*, 8289−8298.

(8) Wang, R.; Tan, H.; Zhao, Z.; Zhang, G.; Song, L.; Dong, W.; Sun, Z. Stable ZnO@TiO_2 Core/Shell Nanorod Arrays with Exposed High Energy Facets for Self-Cleaning Coatings with Anti-Reflective Properties. *J. Mater. Chem. A* **2014**, *2*, 7313−7318.

(9) Yang, T.; Peng, J.; Zheng, Y.; He, X.; Hou, Y.; Wu, L.; Fu, X. Enhanced Photocatalytic Ozonation Degradation of Organic Pollutants by ZnO Modified TiO_2 Nanocomposites. *Appl. Catal., B* **2018**, *221*, 223−234.

(10) Pérez-González, M.; Tomás, S. A.; Santoyo-Salazar, J.; Morales-Luna, M. Enhanced Photocatalytic Activity of TiO_2-ZnO Thin Films Deposited by DC Reactive Magnetron Sputtering. *Ceram. Int.* **2017**, *43*, 8831−8838.

(11) Todorova, N.; Giannakopoulou, T.; Pomoni, K.; Yu, J.; Vaimakis, T.; Trapalis, C. Photocatalytic NO_x Oxidation over Modified ZnO/TiO_2 Thin Films. *Catal. Today* **2015**, *252*, 41−46.

(12) Hernández, S.; Cauda, V.; Hidalgo, D.; Farías Rivera, V.; Manfredi, D.; Chiodoni, A.; Pirri, F. C. Fast and Low-Cost Synthesis of 1D ZnO-TiO_2 Core-Shell Nanoarrays: Characterization and Enhanced Photo-Electrochemical Performance for Water Splitting. *J. Alloys Compd.* **2014**, *615*, S530−S537.

(13) Liu, M.; Nam, C.-Y.; Black, C. T.; Kamcev, J.; Zhang, L. Enhancing Water Splitting Activity and Chemical Stability of Zinc Oxide Nanowire Photoanodes with Ultrathin Titania Shells. *J. Phys. Chem. C* **2013**, *117*, 13396−13402.

(14) Huang, Y.-C.; Chang, S.-Y.; Jehng, J.-M. Photocatalytic H_2 Generation Efficiencies of TiO_2 Nanotube-Based Heterostructures Grafted with ZnO Nanorods, Ag Nanoparticles, or Pd Nanodendrites. *J. Phys. Chem. C* **2017**, *121*, 19063−19068.

(15) Li, Y.; Wang, L.; Liang, J.; Gao, F.; Yin, K.; Dai, P. Hierarchical Heterostructure of ZnO@TiO_2 Hollow Spheres for Highly Efficient Photocatalytic Hydrogen Evolution. *Nanoscale Res. Lett.* **2017**, *12*, 531.

(16) Hernández, S.; Cauda, V.; Chiodoni, A.; Dallorto, S.; Sacco, A.; Hidalgo, D.; Celasco, E.; Pirri, C. F. Optimization of 1D ZnO@TiO_2 Core-Shell Nanostructures for Enhanced Photoelectrochemical Water Splitting under Solar Light Illumination. *ACS Appl. Mater. Interfaces* **2014**, *6*, 12153−12167.

(17) Lou, Y.; Yuan, S.; Zhao, Y.; Hu, P.; Wang, Z.; Zhang, M.; Shi, L.; Li, D. A Simple Route for Decorating TiO_2 Nanoparticle over ZnO Aggregates Dye-Sensitized Solar Cell. *Chem. Eng. J.* **2013**, *229*, 190−196.

(18) Park, K.; Zhang, Q.; Garcia, B. B.; Zhou, X.; Jeong, Y.-H.; Cao, G. Effect of an Ultrathin TiO_2 Layer Coated on Submicrometer-Sized ZnO Nanocrystallite Aggregates by Atomic Layer Deposition on the Performance of Dye-Sensitized Solar Cells. *Adv. Mater.* **2010**, *22*, 2329−2332.

(19) Wang, M.; Huang, C.; Cao, Y.; Yu, Q.; Guo, W.; Liu, Q.; Liang, J.; Hong, M. A Plasma Sputtering Decoration Route to Producing Thickness-Tunable ZnO/TiO_2 Core/Shell Nanorod Arrays. *Nanotechnology* **2009**, *20*, 285311.

(20) Lee, K. M.; Lai, C. W.; Ngai, K. S.; Juan, J. C. Recent Developments of Zinc Oxide Based Photocatalyst in Water Treatment Technology: a Review. *Water Res.* **2016**, *88*, 428−448.

(21) Aggelopoulos, C. A.; Dimitropoulos, M.; Govatsi, A.; Sygellou, L.; Tsakiroglou, C. D.; Yannopoulos, S. N. Influence of the Surface-to-

DOI: 10.1021/acsami.8b22744
ACS Appl. Mater. Interfaces 2019, 11, 15881−15890

Bulk Defects Ratio of ZnO and TiO_2 on their UV-Mediated Photocatalytic Activity. *Appl. Catal., B* **2017**, *205*, 292−301.
(22) Chen, Y.; Zeng, D.; Zhang, K.; Lu, A.; Wang, L.; Peng, D.-L. Au-ZnO Hybrid Nanoflowers, Nanomultipods and Nanopyramids: One-Pot Reaction Synthesis and Photocatalytic Properties. *Nanoscale* **2014**, *6*, 874−881.
(23) Rafiq, M. Y.; Iqbal, F.; Aslam, F.; Bilal, M.; Munir, N.; Sultana, I.; Ashraf, F.; Manzoor, F.; Hassan, N.; Razaq, A. Fabrication and Characterization of ZnO/MnO_2 and ZnO/TiO_2 Flexible Nanocomposites for Energy Storage Applications. *J. Alloys Compd.* **2017**, *729*, 1072−1078.
(24) Boyadjiev, S. I.; Kéri, O.; Bárdos, P.; Firkala, T.; Gáber, F.; Nagy, Z. K.; Baji, Z.; Takács, M.; Szilágyi, I. M. TiO_2/ZnO and ZnO/TiO_2 Core/Shell Nanofibers Prepared by Electrospinning and Atomic Layer Deposition for Photocatalysis and Gas Sensing. *Appl. Surf. Sci.* **2017**, *424*, 190−197.
(25) Momeni, M. M.; Ghayeb, Y. Visible Light-Driven Photoelectrochemical Water Splitting on ZnO-TiO_2 Heterogeneous Nanotube Photoanodes. *J. Appl. Electrochem.* **2015**, *45*, 557−566.
(26) Yang, H. Y.; Yu, S. F.; Lau, S. P.; Zhang, X.; Sun, D. D.; Jun, G. Direct Growth of ZnO Nanocrystals onto the Surface of Porous TiO_2 Nanotube Arrays for Highly Efficient and Recyclable Photocatalysts. *Small* **2009**, *5*, 2260−2264.
(27) Fateh, R.; Dillert, R.; Bahnemann, D. Self-Cleaning Properties, Mechanical Stability, and Adhesion Strength of Transparent Photocatalytic TiO_2-ZnO Coatings on Polycarbonate. *ACS Appl. Mater. Interfaces* **2014**, *6*, 2270−2278.
(28) Li, X.; Wang, C.; Xia, N.; Jiang, M.; Liu, R.; Huang, J.; Li, Q.; Luo, Z.; Liu, L.; Xu, W.; Fang, D. Novel ZnO-TiO_2 Nanocomposite Arrays on Ti Fabric for Enhanced Photocatalytic Application. *J. Mol. Struct.* **2017**, *1148*, 347−355.
(29) Xu, F.; Mei, J.; Li, X.; Sun, Y.; Wu, D.; Gao, Z.; Zhang, Q.; Jiang, K. Heterogeneous Three-Dimensional TiO_2/ZnO Nanorod Array for Enhanced Photoelectrochemical Water Splitting Properties. *J. Nanopart. Res.* **2017**, *19*, 297.
(30) Moradi, S.; Aberoomand-Azar, P.; Raeis-Farshid, S.; Abedini-Khorrami, S.; Givianrad, M. H. The Effect of Different Molar Ratios of ZnO on Characterization and Photocatalytic Activity of TiO_2/ZnO Nanocomposite. *J. Saudi Chem. Soc.* **2016**, *20*, 373−378.
(31) Wu, D.; Gao, Z.; Xu, F.; Shi, Z.; Tao, W.; Jiang, K. Nanosheet-Based Hierarchical ZnO Structure Decorated with TiO_2 Particles for Enhanced Performance in Dye-Sensitized Solar Cell. *CrystEngComm* **2012**, *14*, 7934−7941.
(32) Shi, J. On the Synergetic Catalytic Effect in Heterogeneous Nanocomposite Catalysts. *Chem. Rev.* **2013**, *113*, 2139−2181.
(33) Samadi, M.; Zirak, M.; Naseri, A.; Khorashadizade, E.; Moshfegh, A. Z. Recent Progress on Doped ZnO Nanostructures for Visible-Light Photocatalysis. *Thin Solid Films* **2016**, *605*, 2−19.
(34) Bloh, J. Z. Refined Model for the Optimal Metal Content in Semiconductor Photocatalysts. *J. Phys. Chem. C* **2017**, *121*, 844−851.
(35) Bloh, J. Z.; Dillert, R.; Bahnemann, D. W. Designing Optimal Metal-Doped Photocatalysts: Correlation between Photocatalytic Activity, Doping Ratio, and Particle Size. *J. Phys. Chem. C* **2012**, *116*, 25558−25562.
(36) Karmakar, K.; Sarkar, A.; Mandal, K.; Khan, G. G. Stable and Enhanced Visible-Light Water Electrolysis Using C, N, and S Surface Functionalized ZnO Nanorod Photoanodes: Engineering the Absorption and Electronic Structure. *ACS Sustainable Chem. Eng.* **2016**, *4*, 5693−5702.
(37) Jongprateep, O.; Deedit, P.; Puranasamriddhi, R.; Meesombad, K. Synthesis of Nanoparticulate Ti-doped ZnO by Solution Combustion Technique. *J. Met., Mater. Miner.* **2018**, *28*, 104−108.
(38) Chang, S.-M.; Liu, W.-S. Surface Doping is More Beneficial Than Bulk Doping to the Photocatalytic Activity of Vanadium-Doped TiO_2. *Appl. Catal., B* **2011**, *101*, 333−342.
(39) Ould-Chikh, S.; Proux, O.; Afanasiev, P.; Khrouz, L.; Hedhili, M. N.; Anjum, D. H.; Harb, M.; Geantet, C.; Basset, J. M.; Puzenat, E. Photocatalysis with Chromium-Doped TiO_2: Bulk and Surface Doping. *ChemSusChem* **2014**, *7*, 1361−1371.
(40) Bloh, J. Z.; Dillert, R.; Bahnemann, D. W. Zinc Oxide Photocatalysis: Influence of Iron and Titanium Doping and Origin of the Optimal Doping Ratio. *ChemCatChem* **2013**, *5*, 774−778.
(41) Suwanboon, S.; Amornpitoksuk, P.; Bangrak, P. Synthesis, Characterization and Optical Properties of $Zn_{1-x}Ti_xO$ Nanoparticles Prepared via a High-Energy Ball Milling Technique. *Ceram. Int.* **2011**, *37*, 333−340.
(42) Gasparotto, A.; Barreca, D.; Maccato, C.; Tondello, E. Manufacturing of Inorganic Nanomaterials: Concepts and Perspectives. *Nanoscale* **2012**, *4*, 2813−2825.
(43) Zhang, L.; Jaroniec, M. Toward Designing Semiconductor-Semiconductor Heterojunctions for Photocatalytic Applications. *Appl. Surf. Sci.* **2018**, *430*, 2−17.
(44) Pawar, A. U.; Kim, C. W.; Kang, M. J.; Kang, Y. S. Crystal Facet Engineering of ZnO Photoanode for the Higher Water Splitting Efficiency with Proton Transferable Nafion Film. *Nano Energy* **2016**, *20*, 156−167.
(45) Barreca, D.; Carraro, G.; Maccato, C.; Altantzis, T.; Kaunisto, K.; Gasparotto, A. Controlled Growth of Supported ZnO Inverted Nanopyramids with Downward Pointing Tips. *Cryst. Growth Des.* **2018**, *18*, 2579−2587.
(46) Kuang, Q.; Wang, X.; Jiang, Z.; Xie, Z.; Zheng, L. High-Energy-Surface Engineered Metal Oxide Micro- and Nanocrystallites and Their Applications. *Acc. Chem. Res.* **2014**, *47*, 308−318.
(47) Zeng, J. H.; Jin, B. B.; Wang, Y. F. Facet Enhanced Photocatalytic Effect with Uniform Single-Crystalline Zinc Oxide Nanodisks. *Chem. Phys. Lett.* **2009**, *472*, 90−95.
(48) McLaren, A.; Valdes-Solis, T.; Li, G.; Tsang, S. C. Shape and Size Effects of ZnO Nanocrystals on Photocatalytic Activity. *J. Am. Chem. Soc.* **2009**, *131*, 12540−12541.
(49) Guo, D.; Wang, J.; Cui, C.; Li, P.; Zhong, X.; Wang, F.; Yuan, S.; Zhang, K.; Zhou, Y. ZnO@TiO_2 Core-Shell Nanorod Arrays with Enhanced Photoelectrochemical Performance. *Sol. Energy* **2013**, *95*, 237−245.
(50) Sreedhar, A.; Jung, H.; Kwon, J. H.; Yi, J.; Sohn, Y.; Gwag, J. S. Novel Composite ZnO/TiO_2 Thin Film Photoanodes for Enhanced Visible-Light-Driven Photoelectrochemical Water Splitting Activity. *J. Electroanal. Chem.* **2017**, *804*, 92−98.
(51) Wang, M.; Huang, C.; Cao, Y.; Yu, Q.; Deng, Z.; Liu, Y.; Huang, Z.; Huang, J.; Huang, Q.; Guo, W.; Liang, J. Dye-sensitized solar cells based on nanoparticle-decorated ZnO/TiO_2 core/shell nanorod arrays. *J. Phys. D: Appl. Phys.* **2009**, *42*, 155104.
(52) Barreca, D.; Ferrucci, A. P.; Gasparotto, A.; Maccato, C.; Maragno, C.; Tondello, E. Temperature-Controlled Synthesis and Photocatalytic Performance of ZnO Nanoplatelets. *Chem. Vap. Deposition* **2007**, *13*, 618−625.
(53) Barreca, D.; Carraro, G.; Gasparotto, A.; Maccato, C.; Altantzis, T.; Sada, C.; Kaunisto, K.; Ruoko, T.-P.; Bals, S. Vapor Phase Fabrication of Nanoheterostructures Based on ZnO for Photoelectrochemical Water Splitting. *Adv. Mater. Interfaces* **2017**, *4*, 1700161.
(54) Schlossmacher, P.; Klenov, D. O.; Freitag, B.; von Harrach, H. S. Enhanced Detection Sensitivity with a New Windowless XEDS System for AEM Based on Silicon Drift Detector Technology. *Microsc. Today* **2010**, *18*, 14−20.
(55) Warwick, M. E. A.; Kaunisto, K.; Barreca, D.; Carraro, G.; Gasparotto, A.; Maccato, C.; Bontempi, E.; Sada, C.; Ruoko, T.-P.; Turner, S.; Van Tendeloo, G. Vapor Phase Processing of α-Fe_2O_3 Photoelectrodes for Water Splitting: An Insight into the Structure/Property Interplay. *ACS Appl. Mater. Interfaces* **2015**, *7*, 8667−8676.
(56) Barreca, D.; Gri, F.; Gasparotto, A.; Carraro, G.; Bigiani, L.; Altantzis, T.; Žener, B.; Lavrenčič Štangar, U.; Alessi, B.; Padmanaban, D. B.; Mariotti, D.; Maccato, C. Multi-functional MnO_2 Nanomaterials for Photo-Activated Applications by a Plasma-Assisted Fabrication Route. *Nanoscale* **2019**, *11*, 98−108.
(57) ISO 27448: *Fine Ceramics, Advanced Technical Ceramics - Test Method for Self-Cleaning Performance of Semiconducting Photocatalytic Materials - Measurement of Water Contact Angle*; ISO: Geneva, 2009.

DOI: 10.1021/acsami.8b22744
ACS Appl. Mater. Interfaces 2019, 11, 15881−15890

(58) Mills, A.; Hill, C.; Robertson, P. K. J. Overview of the Current ISO Tests for Photocatalytic Materials. *J. Photochem. Photobiol., A* **2012**, *237*, 7−23.
(59) Soklič, A.; Tasbihi, M.; Kete, M.; Lavrenčič Štangar, U. Deposition and Possible Influence of a Self-Cleaning Thin TiO_2/SiO_2 Film on a Photovoltaic Module Efficiency. *Catal. Today* **2015**, *252*, 54−60.
(60) Vodišek, N.; Ramanujachary, K.; Brezová, V.; Lavrenčič Štangar, U. Transparent Titania-Zirconia-Silica Thin Films for Self-Cleaning and Photocatalytic Applications. *Catal. Today* **2017**, *287*, 142−147.
(61) Žener, B.; Matoh, L.; Carraro, G.; Miljević, B.; Cerc Korošec, R. Sulfur-, Nitrogen- and Platinum-Doped Titania Thin Films with High Catalytic Efficiency under Visible-Light Illumination. *Beilstein J. Nanotechnol.* **2018**, *9*, 1629−1640.
(62) Pattern No. 36-1451; JCPDS, 2000.
(63) Balbuena, J.; Carraro, G.; Cruz, M.; Gasparotto, A.; Maccato, C.; Pastor, A.; Sada, C.; Barreca, D.; Sánchez, L. Advances in Photocatalytic NO_x Abatement through the Use of Fe_2O_3/TiO_2 Nanocomposites. *RSC Adv.* **2016**, *6*, 74878−74885.
(64) Barreca, D.; Carraro, G.; Gasparotto, A.; Maccato, C.; Sada, C.; Bontempi, E.; Brisotto, M.; Pliekhova, O.; Lavrenčič Štangar, U. Novel Two-Step Vapor-Phase Synthesis of UV-Vis Light Active Fe_2O_3/WO_3 Nanocomposites for Phenol Degradation. *Environ. Sci. Pollut. Res.* **2016**, *23*, 20350−20359.
(65) Krylova, G.; Brioude, A.; Ababou-Girard, S.; Mrazek, J.; Spanhel, L. Natural Superhydrophilicity and Photocatalytic Properties of Sol-Gel Derived $ZnTiO_3$-Ilmenite/r-TiO_2 Films. *Phys. Chem. Chem. Phys.* **2010**, *12*, 15101−15110.
(66) Fittipaldi, M.; Gombac, V.; Gasparotto, A.; Deiana, C.; Adami, G.; Barreca, D.; Montini, T.; Martra, G.; Gatteschi, D.; Fornasiero, P. Synergistic Role of B and F Dopants in Promoting the Photocatalytic Activity of Rutile TiO_2. *ChemPhysChem* **2011**, *12*, 2221−2224.
(67) Smirnova, N.; Gnatyuk, Y.; Vityuk, N.; Linnik, O.; Eremenko, A.; Vorobets, V.; Kolbasov, G. Nanosized TiO_2 - Based Mixed Oxide Films: Sol-Gel Synthesis, Structure, Electrochemical Characteristics and Photocatalytic Activity. *Int. J. Mater. Eng.* **2013**, *3*, 124−135.
(68) Chen, Y.; Zhang, C.; Huang, W.; Yang, C.; Huang, T.; Situ, Y.; Huang, H. Synthesis of Porous ZnO/TiO_2 Thin Films with Superhydrophilicity and Photocatalytic Activity via a Template-Free Sol-Gel Method. *Surf. Coat. Technol.* **2014**, *258*, 531−538.
(69) Salvador, P. The Influence of Niobium Doping on the Efficiency of n-TiO_2 Electrode in Water Photoelectrolysis. *Sol. Energy Mater.* **1980**, *2*, 413−421.
(70) Kim, H.; Auyeung, R. C. Y.; Ollinger, M.; Kushto, G. P.; Kafafi, Z. H.; Piqué, A. Laser-Sintered Mesoporous TiO_2 Electrodes for Dye-Sensitized Solar Cells. *Appl. Phys. A: Mater. Sci. Process.* **2006**, *83*, 73−76.
(71) Manoj, P. K.; Koshy, P.; Vaidyan, V. K. Transparent Anatase Titania Films: A Critical Study on Optical Properties. *Prog. Nat. Sci.* **2012**, *22*, 79−85.
(72) Yoshikawa, H.; Adachi, S. Optical Constants of ZnO. *Jpn. J. Appl. Phys., Part 1.* **1997**, *36*, 6237−6243.
(73) Hu, Z.; Herrera Santos, J. F.; Oskam, G.; Searson, P. C. Influence of the Reactant Concentrations on the Synthesis of ZnO Nanoparticles. *J. Colloid Interface Sci.* **2005**, *288*, 313−316.
(74) Podsiadły-Paszkowska, A.; Tranca, I.; Szyja, B. M. Tuning the Hematite (110) Surface Properties To Enhance Its Efficiency in Photoelectrochemistry. *J. Phys. Chem. C* **2019**, *123*, 5401−5410.
(75) Cheng, J.; Wang, P.; Hua, C.; Yang, Y.; Zhang, Z. The Impact of Iron Adsorption on the Electronic and Photocatalytic Properties of the Zinc Oxide (0001) Surface: A First-Principles Study. *Materials* **2018**, *11*, 417.
(76) Ivanov, I.; Pollmann, J. Electronic Structure of Ideal and Relaxed Surfaces of ZnO: A Prototype Ionic Wurtzite Semiconductor and its Surface Properties. *Phys. Rev. B: Condens. Matter Mater. Phys.* **1981**, *24*, 7275−7296.
(77) Kelly, L. L.; Racke, D. A.; Schulz, P.; et al. Spectroscopy and Control of Near-Surface Defects in Conductive Thin Film ZnO. *J. Phys.: Condens. Matter* **2016**, *28*, 094007.
(78) Harsdorff, M. Heterogeneous Nucleation and Growth of Thin Films. *Thin Solid Films* **1982**, *90*, 1−14.
(79) Wender, H.; Migowski, P.; Feil, A. F.; Teixeira, S. R.; Dupont, J. Sputtering Deposition of Nanoparticles onto Liquid Substrates: Recent Advances and Future Trends. *Coord. Chem. Rev.* **2013**, *257*, 2468−2483.
(80) *PVD for Microelectronics, Sputter Deposition Applied to Semiconductor Manufacturing*; Powell, R. A., Rossnagel, S. M., Eds.; Elsevier: 1999; Vol. *26*, Chapter 2, pp 23−49.
(81) Afroz, K.; Moniruddin, M.; Bakranov, N.; Kudaibergenov, S.; Nuraje, N. A Heterojunction Strategy to Improve the Visible Light Sensitive Water Splitting Performance of Photocatalytic Materials. *J. Mater. Chem. A* **2018**, *6*, 21696−21718.

DOI: 10.1021/acsami.8b22744
ACS Appl. Mater. Interfaces 2019, 11, 15881−15890